

1 **Model assessment of the observed relationship between El Niño and the**
2 **northern East Asian summer monsoon using the CCSM Community**
3 **Atmosphere Model-Community Land Model version 3 (CAM-CLM3)**

4
5 Eungul Lee^{1,2,4}, Thomas N. Chase^{1,3}, Peter J. Lawrence¹, and Balaji Rajagopalan^{1,3}

6
7 ¹ Cooperative Institute for Research in Environmental Sciences (CIRES),
8 University of Colorado, Boulder, Colorado, USA

9 ² Department of Geography, University of Colorado, Boulder, Colorado, USA

10 ³ Department of Civil, Environmental, and Architectural Engineering, University of
11 Colorado, Boulder, Colorado, USA

12 ⁴ Center for Sustainability and the Global Environment (SAGE), University of Wisconsin,
13 Madison, Wisconsin, USA

14
15 **Abstract**

16 Plausibility and reproducibility of the relationship and physical mechanisms
17 proposed between the northern East Asian summer monsoon (NEASM) and El Niño are
18 verified and illuminated using the Community Climate System Model (CCSM) with the
19 Community Atmosphere Model-Community Land Model version 3 (CAM-CLM3).
20 The climate responses over East Asia and western North Pacific to El Niño are simulated
21 in the CCSM3 using dynamic atmosphere and land with prescribed climatological and El
22 Niño sea surface temperature (SST) anomalies. A significantly intensified NEASM is
23 simulated for the El Niño experiments, which validates the positive correlation between
24 NEASM precipitation and El Niño found in recent observational analysis. Analysis of
25 lower-level wind vector and vorticity in the model experiments elucidates the physical
26 mechanism behind the positive correlation between NEASM precipitation and El Niño,
27 and shows that the western North Pacific anticyclone plays an important role in the
28 connection between the NEASM and the tropical SST anomalies.

29 **1. Introduction**

30 Many studies have focused on the relationships between the East Asian summer
31 monsoon (EASM) and sea surface temperatures (SSTs) in the Pacific and Indian Oceans
32 [e.g., *Shen and Lau, 1995; Zhang et al., 1996; Wang et al., 2000; Chang et al., 2000a, b;*
33 *Wu and Wang, 2002; Wang and Li, 2004; Lee et al., 2005; Hsu and Lin, 2007; Lee et al.,*
34 *2008*], because SSTs influence the atmosphere through surface heat fluxes, mainly latent
35 heating [*Wu and Newell, 1998*]. The variability of SST in the tropical Pacific and
36 adjacent regions (i.e. El Niño/Southern Oscillation) is correlated with summer rainfall in
37 the EASM region, covering eastern China, the Korean peninsula, Japan, and the adjacent
38 marginal seas [*Shen and Lau, 1995; Zhang et al., 1996; Wu and Wang, 2002; Lee et al.,*
39 *2005; Lee et al., 2008*]. Previously, in an observational analysis, we found northern
40 EASM (NEASM over 30°~50°N and 110°~145°E; see Fig. 3a) precipitation is positively
41 correlated with SST in the tropical eastern Pacific and Indian Ocean, and negatively
42 correlated with SST in the tropical western Pacific [*Lee et al., 2008*]. That paper
43 proposed plausible physical linkages between tropical SST anomalies and the NEASM
44 with a stronger NEASM related to enhanced western North Pacific (WNP) anticyclonic
45 anomalies and thus more cyclonic anomalies in the NEASM region due to the Pacific-
46 East Asian teleconnection [*Wang et al., 2000*], which is connected to tropical SST

47 anomalies.

48 In our study, we explore the relation between the NEASM and El Niño in model
49 simulations, and elucidate the physical mechanisms governing monsoon strength and
50 seasonality using the Community Climate System Model (CCSM) with the Community
51 Atmosphere Model-Community Land Model version 3 (CAM-CLM3) [*Collins et al.*,
52 2006]. Previous general circulation model (GCM) simulations have poorly reproduced
53 the observed Asian summer monsoon rainfall, particularly in East Asia [*Lau et al.*, 1996;
54 *Kang et al.*, 2002; *Wang et al.*, 2004]. However, CCSM-CAM3 is known for reasonable
55 simulation of the major features of the global hydrological cycle [*Hack et al.*, 2006].
56 *Meehl et al.* [2006] examined aspects of regional monsoon regimes (but not including the
57 NEASM) in the CCSM3 with the CAM3. In their study, they concluded that most of
58 the major 850 hPa wind characteristics in the monsoon regimes are well represented in
59 the CCSM3, with associated regional monsoon precipitation maxima. Here, we analyze
60 the CCSM3 with the CAM-CLM3 in both its ability to reproduce NEASM circulation
61 patterns and rainfall and the model response to El Niño. We are investigating the
62 response of the coupled atmosphere and land models to forcing from El Niño SST
63 compared to climatological SST.

64

65 **2. Methods and data**

66 **2.1. Model description and experiments**

67 The CCSM3 framework allows combinations of dynamic or prescribed data
68 models to be used for any of the model components. In our case we are using the
69 dynamic atmosphere and land with prescribed SSTs and sea ice distributions, which have
70 the equivalent physics of the CAM-CLM3 model. In the model El Niño experiments
71 the Data Ocean Model (DOCN6), with annually cycling SSTs, is used to simulate the
72 monthly forcing from SSTs of an average El Niño compared to the standard 1949~2001
73 monthly climatology. The monthly average El Niño SST anomalies are generated from
74 the Hadley Center monthly SST data [Rayner *et al.*, 2003], using anomalies for all
75 months that had seasonal averaged SST in the Niño 1, 2 and 3 regions warmer than 1°C
76 above climatology for the 1900~2003 period (Fig. 1). The monthly El Niño SST
77 anomalies are added to the climatology SST parameters for use in the DOCN6 model.
78 The climate responses to the El Niño SST anomalies are simulated in the CCSM3
79 through the CAM3, and with the CLM3 using the new Moderate Resolution Imaging
80 Spectroradiometer (MODIS) land surface parameters from Lawrence and Chase [2007]
81 and using the new CLM SiB surface hydrology described in Lawrence and Chase [In
82 press], which is used in all experiments to avoid the problems of evapo-transpiration

83 partition and surface hydrology found with the standard release of CLM 3.0. Sea ice
84 distributions are prescribed from the 1949~2005 monthly climatology for all experiments
85 using the Community Sea Ice Model version 5 (CSIM5).

86 We perform four experiments using 30-year equilibrium simulations throwing out
87 the first 5 years as spin up from each simulation. The model experiments are: (i) three
88 control runs of the CAM-CLM3 with a different initial condition and (ii) a single run
89 using average El Niño SST anomalies. Differences in initial conditions between each
90 realization of the ensemble are set by randomly increasing or decreasing the surface
91 temperature of all land grid cells by $\pm 0.1^\circ\text{C}$. We combine three control runs to estimate
92 model variability, and use the combined control run (75 years) to compare with the El
93 Niño run (25 years). Spatial resolution of the CAM3 is a 26-level 42-wave triangular
94 spectral truncation (T42 L26) of the atmospheric physics, but all parameter and history
95 files are run on a rectangular geographic grid of 64×128 cells which equates to
96 $2.8125^\circ \times 2.8125^\circ$ (actually there is a pole offset of the grid which makes the latitude
97 spacing slightly smaller). The CLM3 is run on the same rectangular grid as the CAM3.
98 The DOCN6 and CSIM5 models are both run on a 180×360 domain which equates to
99 $1^\circ \times 1^\circ$. For the comparisons of the model with observed results, the resolution of the
100 model output is regridded to that of observation (i.e. $2.5^\circ \times 2.5^\circ$)

101 **2.2. Data and statistical methods**

102 To compare the CAM-CLM3 results with observations, we use observed
103 precipitation (mm/day) derived from the version-2 Global Precipitation Climatology
104 Project (GPCP) monthly precipitation [*Adler et al.*, 2003], and mean sea level pressure
105 [SLP (hPa)], 500 hPa geopotential height [HGT (gpm)], 150 hPa divergence [DIV (s^{-1})]
106 and 850 hPa wind vector (m/s) and vorticity (s^{-1}) calculated with mean 150 and 850 hPa,
107 respectively, u - and v -winds (m/s) from the National Centers for Environmental
108 Prediction-Department of Energy (NCEP-DOE) Atmospheric Model Intercomparison
109 Project (AMIP-II) monthly reanalysis [*Kanamitsu et al.*, 2002]. GPCP version-2
110 precipitation is a globally complete, monthly analysis of surface precipitation at
111 $2.5^{\circ} \times 2.5^{\circ}$ resolution available from January 1979 to the present. It is a merged analysis
112 that incorporates precipitation estimates from low-orbit satellite microwave data,
113 geosynchronous-orbit satellite infrared data, and surface rain gauge observations [*Adler*
114 *et al.*, 2003]. SLP, 500 hPa HGT, 150 hPa DIV, and 850 hPa wind vector and vorticity
115 from the NCEP-DOE AMIP-II reanalysis are strongly influenced by observed data
116 [*Kalnay et al.*, 1996]. We use the NCEP-DOE AMIP-II reanalysis as fixes to known
117 processing errors in the NCEP-NCAR (National Center for Atmospheric Research)
118 reanalysis have been incorporated and it uses an improved forecast model and data

119 assimilation system [*Kanamitsu et al.*, 2002]. Spatial and temporal resolutions of the
120 reanalysis are consistent with those of the GPCP precipitation. In this study, a 25-year
121 climatology for 1979~2003 is used to compare with the model results from control and
122 El Niño simulations.

123 In order to check if there is significant correlation in the spatial patterns between
124 CAM-CLM3 control and observed climatology, we compute the spatial correlation
125 coefficients between the model and observations based on each grid points in the
126 specified region (i.e., globe or NEASM region). A Student's *t*-test is conducted to
127 quantify the statistical significance of the difference of means between El Niño and
128 normal years (i.e. climatology SST) from the simulated and observed variables (i.e.,
129 precipitation, 150 hPa DIV, SLP, and 500 hPa HGT). We use the *t*-statistic for unequal
130 population variances, because the *F* tests for the variances of the two-samples show
131 significant differences (at the 90% level; not shown here) in some regions over East Asia
132 and the WNP (10°~60°N and 100°~190°E). Significant regions at the 90 and 95%
133 levels are contoured. The relationship between NEASM precipitation and El Niño
134 during the pre-monsoon season (December through May) is examined using a statistical
135 forecast model of *Lee et al.* [2008] (Equation 1).

136

137 $NEASM\ precipitation = 2.6 - 0.51\ SST\ in\ the\ TEP - 1.28\ SST\ in\ the\ TWP$
138 $+ 1.17\ SST\ in\ the\ TIO + 0.68\ OHC\ in\ the\ TIO \quad (1)$

139 where *SST in the TEP* is SST in the tropical eastern Pacific (5°S~5°N,
140 170°~80°W), *SST in the TWP* is SST in the tropical western Pacific (0°~15°N,
141 130°~160°E), *SST in the TIO* is SST in the tropical Indian Ocean (10°S~10°N,
142 40°~100°E), and *OHC in the TIO* is ocean heat content in the tropical Indian Ocean
143 (20°S~15°N, 50°~70°E) during the pre-monsoon season.

144 We calculate NEASM precipitation using a statistical model where the predictors
145 in the forecast model (SSTs and OHC) are averaged over the specified regions in the
146 model runs during the pre-monsoon season. The difference between NEASM
147 precipitation for the El Niño simulation versus the control simulation is compared with
148 that from observed Hadley Center SST during El Niño years versus normal years. We
149 also calculate NEASM precipitation simulated in the CAM-CLM3 runs.

150

151 **3. Comparisons of CAM-CLM3 control run with observations**

152 Fig. 2a and b show the zonal and spatial distributions of annual precipitation
153 from the CAM-CLM3 control simulations and 1979~2003 GPCP climatology. In order
154 to check if there is significant correlation between the distributions, we calculate the

155 spatial pattern correlation between model and observational precipitation over the globe
156 (6,048 data points). Annual precipitation from the CAM-CLM3 is significantly
157 correlated with that from GPCP ($r=0.79$; $p\text{-value}<0.01$). The tropical precipitation in
158 the intertropical convergence zone (ITCZ) is generally well captured, which is shown in
159 two peaks, although there is a more exaggerated ITCZ in the CAM-CLM3 than in GPCP
160 (Fig. 2a). This is due to overestimated precipitation in the tropical Indian and Pacific
161 Oceans between $30^{\circ}\text{S}\sim 30^{\circ}\text{N}$ except for equatorial region. (Bottom plot in Fig. 2b;
162 Horizontal distributions and differences of seasonal mean precipitation are shown in
163 Figure S1 in the auxiliary material.). Subtropical precipitation minima (subtropical
164 High) are generally displaced poleward about 10° , and the secondary precipitation
165 maxima (midlatitude frontal precipitation) are shifted equatorward in the southern
166 hemisphere and poleward in the northern hemisphere (Fig. 2a).

167 Comparisons of CAM-CLM3 with observed variables over East Asia and the
168 WNP are shown in Fig. 3. During June through August (JJA), precipitation from the
169 control simulations is overestimated over the subtropical North Pacific (i.e., $10^{\circ}\sim 30^{\circ}\text{N}$
170 and $150^{\circ}\text{E}\sim 170^{\circ}\text{W}$) and underestimated over the NEASM region (Fig. 3a) relative to that
171 from observations. CAM-CLM3 cannot reproduce the observed rain band in the
172 NEASM region, which is due to an unrealistic dry zone over the Korean peninsula and

173 Japan extending to the northwestern Pacific. This problem has been mentioned in
174 previous GCM intercomparison studies [e.g., *Lau et al.*, 1996; *Kang et al.*, 2002]
175 indicating the general model difficulty in simulating regional precipitation. Observed
176 precipitation data may also not be highly reliable due to its high spatial variability, the
177 lack of rain gauges, especially over oceanic and unpopulated land areas, and the
178 uncertainties and inhomogeneity in the satellite observations [e.g., *Lau et al.*, 1996; *Xie*
179 *and Arkin*, 1997; *Adler et al.*, 2003]. Therefore, we use observed variables which are
180 smoother, better observed and therefore more reliable than precipitation for comparison
181 with model results. These include 150 hPa DIV, SLP, 500 hPa HGT, and 850 hPa wind
182 and vorticity, which are class A variables (i.e. most reliable) from reanalysis [*Kalnay et*
183 *al.*, 1996].

184 JJA upper-level divergence zone is used as an NEASM index, which coincides
185 with the lower-level convergence zone of the summer monsoon [e.g., *Lee et al.*, 2008].
186 JJA 150 hPa DIV from the control runs reproduces the observed monsoon band in the
187 NEASM region, though it is overestimated over the subtropical North Pacific and
188 underestimated over the southern EASM region (20°~30°N and 110°~145°E) (Fig. 3b).
189 The spatial distributions of averaged JJA SLP, 500 hPa HGT, and 850 hPa wind and
190 vorticity are shown in Figs. 3c, d, and e. Simulated spatial patterns of SLP, 500 hPa

191 HGT, and 850 hPa vorticity over the NEASM region (135 data points) are significantly
192 correlated with those from NCEP-DOE AMIP-II ($r=0.90$, 0.96 and 0.37 , respectively; all
193 p -values <0.01). Vorticity is calculated with u - and v -winds using finite differencing at
194 each grid point, which tends to make it less smooth than SLP and HGT. It might be one
195 of the reasons why the correlation value of 850 hPa vorticity is smaller relative to those
196 of SLP and 500 hPa HGT. Simulated SLP shows high-pressure center over the North
197 Pacific, which is one of the important dynamic mechanisms in the NEASM circulation
198 [e.g., *Wang et al.*, 2000], although its magnitude is overestimated in comparisons with
199 NCEP-DOE SLP (Fig. 3c). Relatively low pressure during JJA over East Asia occurs in
200 both model and observation. The spatial pattern of 500 hPa HGT from the CAM-
201 CLM3 shows good agreement with that from observation ($r=0.96$; Fig. 3d). However,
202 the 500 hPa HGT in the control model simulation over the WNP is shifted northward and
203 pressure is too high. Simulated 850 hPa wind vector and vorticity, which are used to
204 elucidate the physical mechanisms between the NEASM and El Niño in the next section,
205 also generally capture the lower level wind and vorticity patterns over East Asia and the
206 WNP (Fig. 3e). The strong negative vorticity in the WNP (i.e. WNP anticyclonic
207 circulation) is displaced poleward about 10° in the model, but is of similar magnitude to
208 the observed circulation. This displacement affects the northern extent of the

209 climatological southwesterly airflow into the NEASM region from the South China Sea
210 and tropical western Pacific shifting precipitation to north. This shift partially explains
211 the weaker model precipitation than observed precipitation in the NEASM region (Fig.
212 3a).

213

214 **4. El Niño sensitivity simulations**

215 Fig. 4 shows the simulated differences of precipitation, 150 hPa DIV, SLP, and
216 500 hPa HGT between El Niño and control runs (left panels), and the observed
217 differences of those variables between the five years of highest SST anomalies in the
218 tropical eastern Pacific covering the Niño 1, 2, and 3 regions, which is consistent with the
219 El Niño definition in the model, and normal year (25-year mean) (right panels).
220 Simulated pattern in Fig. 4a (left panel) demonstrates that JJA precipitation for the El
221 Niño run is higher than that for the control run in the NEASM region with significant
222 positive precipitation over the monsoon band in the NEASM region. The observed
223 pattern (right panel in Fig. 4a) reveals more precipitation over the NEASM region during
224 the years of high SST in the tropical eastern Pacific (i.e. El Niño year), consistent with
225 the simulated pattern (left panel in Fig. 4a). On the other hand, JJA precipitation in the
226 southern EASM region for the El Niño simulation is significantly less than that for the

227 control simulation. As mentioned in section 3, summer precipitation from the CAM-
228 CLM3 control cannot reproduce the observed summer rainfall in the NEASM region.
229 Thus, we examine the impact of El Niño on the NEASM using 150 hPa DIV, SLP and
230 500 hPa HGT, and check if there is the consistency between the results from precipitation
231 and more reliable variables. The simulated difference of 150 hPa DIV between El Niño
232 and control simulations shows a significant positive value in the NEASM region over
233 30°~45°N (left panel in Fig. 4b), consistent with the observed 150 hPa DIV difference in
234 the NEASM region (right panel in Fig. 4b). The simulated distributions of SLP (left
235 panel in Fig. 4c) and 500 hPa HGT (left panel in Fig. 4d) show negative differences in
236 the NEASM region when subtracting the values of the control run from the El Niño run.
237 Negative values of SLP and 500 hPa HGT in the NEASM region are also shown in the
238 observed differences (right panels in Figs.4c and d). These model and observational
239 results using both precipitation and more reliable variables support a stronger NEASM
240 during El Niño.

241 To examine the positive correlation between NEASM precipitation and El Niño
242 during the pre-monsoon season, we calculate NEASM precipitation using a statistical
243 forecast model (Equation 1 in section 2.2) using El Niño and control SST parameters in
244 the model. El Niño year is defined using the averaged SST anomalies in Niño 1, 2 and

245 3 regions for the pre-monsoon season that are warmer than 1°C above climatology SST
246 for the 1900~2003 period. NEASM precipitation is calculated from SSTs in the tropical
247 eastern Pacific, tropical western Pacific and tropical Indian Ocean, and OHC in the
248 tropical Indian Ocean during the pre-monsoon season. Because the CAM-CLM3
249 simulations were run with climatological SSTs, OHC is not available for our analysis.
250 We, therefore, use area-averaged SST over the same area as a proxy for OHC, which is
251 significantly correlated with area-averaged OHC ($r=0.60$; $p\text{-value}<0.01$). Using model
252 SST parameters during the pre-monsoon season, NEASM precipitation during El Niño
253 increases relative to the control (5.14 versus 5.06 mm/day). The difference (+0.08
254 mm/day) is comparable to that from observations (+0.14 mm/day). The difference in
255 NEASM precipitation in the dynamic CAM-CLM3 between El Niño and control
256 simulations is +0.05 mm/day. Therefore, these results are consistent with the previous
257 observational analysis, which showed that a significant positive correlation between
258 NEASM precipitation and El Niño during the pre-monsoon season [Lee *et al.*, 2008].
259 They also support the conclusion that model SST parameters effectively produce ocean
260 forcing for the statistical model of NEASM precipitation, and CAM-CLM3 dynamics
261 reproduce precipitation result established with the statistical model.

262 In order to elucidate the physical mechanisms between the NEASM and El Niño

263 shown in the observational analysis [Lee *et al.*, 2008], we examine mean JJA differences
264 in 850 hPa wind vector and vorticity between the El Niño and control simulations (left
265 panel in Fig. 5). For the El Niño run (i.e. warm SST anomalies in the tropical eastern
266 Pacific), there are cold SST anomalies in the tropical western Pacific, WNP, and western
267 South Pacific (a horseshoe pattern (see Fig. 1)). Cold SST anomalies in the WNP lead
268 to weaker local atmospheric convection and thus a stronger WNP anticyclonic circulation.
269 The stronger WNP anticyclonic circulation further leads to intensified southwesterly
270 flows into the NEASM region which lead to an anomalously strong monsoonal
271 circulation in the region (left panel in Fig. 5), because the southwesterly flows
272 originating in the Indian monsoon region and northern Australia and its neighboring sea
273 regions are the dominant heat and moisture sources for the NEASM [e.g., *Yihui*, 1994].
274 This results in more NEASM precipitation (left panel in Fig. 4a). This result supports
275 the positive relation between the NEASM and El Niño shown in the model simulations as
276 well as observational analyses (Fig. 4). This result also supports the idea that the WNP
277 anticyclone plays an important role in the connection between the NEASM and tropical
278 Pacific SSTs [e.g., *Wang et al.*, 2000; *Chang et al.*, 2000a, b; *Wang and Li*, 2004; *Lee et*
279 *al.*, 2005; *Lee et al.*, 2008]. Simulated spatial pattern in Fig. 5 (left panel) is
280 significantly correlated (p -value<0.01) with observational composite differences of mean

281 JJA 850 hPa wind vector and vorticity for the five years of both highest and of lowest of
282 SST anomalies in the tropical eastern Pacific shown in *Lee et al.* [2008] (right panel in
283 Fig. 5). Thus, this result validates a conclusion that oceanic heat sources in the tropical
284 Pacific can impact the NEASM through the intensity of WNP anticyclonic anomalies
285 proposed by *Lee et al.* [2008].

286

287 **5. Conclusions**

288 CAM-CLM3 is used to assess the physical relationship between the NEASM and
289 SST anomalies during El Niño observed in *Lee et al.* [2008]. The spatial patterns of the
290 differences of precipitation, 150 hPa DIV, SLP, and 500 hPa HGT between the El Niño
291 and control simulations validate the positive correlation between the NEASM and El
292 Niño supporting a stronger NEASM during an El Niño year. We elucidate the physical
293 linkages between the NEASM and tropical SST anomalies proposed in the observational
294 analysis that a stronger NEASM is related to above-normal WNP anticyclonic anomalies
295 and thus more cyclonic anomalies in the NEASM region due to the Pacific-East Asian
296 teleconnection, which is connected to tropical SST anomalies: warm SST anomalies in
297 the tropical eastern Pacific (i.e. El Niño) → cold SST anomalies in the tropical western
298 Pacific, WNP, and western South Pacific → a weaker local atmospheric convection in

299 WNP → a stronger WNP anticyclonic circulation → intensified southwesterly flowing
300 into the NEASM region → an anomalously strong monsoonal circulation → more
301 NEASM precipitation. The intensity of cyclonic circulation in the NEASM region can
302 also affect that of WNP anticyclone, because the two regional circulations are linked by
303 anomalously stronger westerly airflows around 30°N during El Niño (Fig. 5) through a
304 plausible positive feedback. So, what extent NEASM affects the WNP anticyclone
305 needs to be investigated in future study using observational and modeling studies.

306 CAM-CLM3 does a good job at representing the spatial patterns of precipitation
307 over the globe and regional atmospheric dynamic fields (i.e., 150 hPa DIV, SLP, 500 hPa
308 HGT, and 850 hPa vorticity) over the NEASM region, although with some differences
309 from observations. However, CAM-CLM3 poorly reproduces summer precipitation
310 over East Asia similar to other models as shown in previous intercomparison studies.
311 We therefore used broad circulation statistics as our comparison metric.

312

313

314

315

316

317 **Acknowledgements**

318 We wish to thank the anonymous reviewers for valuable suggestions. The first author
319 is thankful to Department of Geography, University of Colorado for the Gilbert F.
320 White Doctoral Fellowship. Partial supports of this work by National Science
321 Foundation via ATM-0437538 and ATM-0639838 grants are also thankfully
322 acknowledged.

323

324 **References**

- 325 Adler, R. F., G. J. Huffman, A. Chang, R. Ferraro, P-P. Xie, J. Janowiak, B. Rudolf, U.
326 Schneider, S. Curtis, D. Bolvin, A. Gruber, J. Susskind, P. Arkin, and E. Nelkin
327 (2003), The version-2 global precipitation climatology project (GPCP) monthly
328 precipitation analysis (1979–present), *J. Hydrometeor.*, *4*, 1147–1167.
- 329 Chang, C.-P., Y. Zhang, and T. Li (2000a), Interannual and interdecadal variations of the
330 East Asian summer monsoon and tropical Pacific SSTs. Part I : Roles of the
331 subtropical ridge, *J. Clim.*, *13*, 4310–4325.
- 332 Chang, C.-P., Y. Zhang, and T. Li (2000b), Interannual and interdecadal variations of the
333 East Asian summer monsoon and tropical Pacific SSTs. Part II: Meridional
334 structure of the monsoon, *J. Clim.*, *13*, 4326–4340.
- 335 Collins, W. D., Coauthors (2006), The Community Climate System Model version 3
336 (CCSM3), *J. Clim.*, *19*, 2122–2143.
- 337 Hack, J. J., J. M. Caron, S. G. Yeager, K. W. Oleson, M. M. Holland, J. E. Truesdale, and
338 P. J. Rasch (2006), Simulation of the global hydrological cycle in the CCSM

339 Community Atmosphere Model version 3 (CAM3): Mean features, *J. Clim.*, 19,
340 2199–2221.

341 Hsu, H.-H., and S.-M. Lin (2007), Asymmetry of the tropical rainfall pattern during the
342 East Asian summer, *J. Clim.*, 20, 4443–4458.

343 Kalnay, E., M. Kanamitsu, R. Kistler, W. Collins, D. Deaven, L. Gandin, M. Iredell, S.
344 Saha, G. White, J. Woollen, Y. Zhu, M. Chelliah, W. Ebisuzaki, W. Higgins, J.
345 Janowiak, K. C. Mo, C. Ropelewski, J. Wang, A. Leetmaa, R. Reynolds, R. Jenne,
346 and D. Joseph (1996), The NCEP/NCAR 40-year reanalysis project, *Bull. Am.*
347 *Meteorol. Soc.*, 77, 437–471.

348 Kanamitsu, M., W. Ebisuzaki, J. Woollen, S.-K. Yang, J. J. Hnilo, M. Fiorino, and G.
349 L. Potter (2002), NCEP-DOE AMIP-II reanalysis (R-2), *Bull. Am. Meteorol. Soc.*,
350 83, 1631–1643.

351 Kang, I.-S., K. Jin, B. Wang, K.-M. Lau, J. Shukla, V. Krishnamurthy, S. D. Schubert, D.
352 E. Wailser, W. F. Stern, A. Kitoh, G. A. Meehl, M. Kanamitsu, V. Y. Galin, V.
353 Satyan, C.-K. Park, and Y. Liu (2002), Intercomparison of the climatological
354 variations of Asian summer monsoon precipitation simulated by 10 GCMs, *Clim.*
355 *Dyn.*, 19, 383–395.

356 Lau, K.-M., J. H. Kim, and Y. Sud (1996), Intercomparison of hydrologic processes in
357 AMIP GCMs, *Bull. Amer. Meteor. Soc.*, 77, 2209–2227.

358 Lawrence, P. J., and T. N. Chase (2007), Representing a new MODIS consistent land
359 surface in the Community Land Model (CLM 3.0), *J. Geophys. Res.*, 112,
360 G01023, doi:10.1029/2006JG000168.

361 Lawrence, P. J., and T. N. Chase (In press), Climate Impacts of making the hydrology of
362 the Community Land Model (CLM 3.0) consistent with the Simple Biosphere

363 Model (SiB 2.0), *J. Hydrometeorology*.

364 Lee, E.-J., J.-G. Jhun, and C.-K. Park (2005), Remote connection of the northeast Asian
365 summer rainfall variation revealed by a newly defined monsoon index, *J. Clim.*,
366 *18*, 4381–4393.

367 Lee, E., T. N. Chase, and B. Rajagopalan (2008), Seasonal forecasting of East Asian
368 summer monsoon based on oceanic heat sources, *Int. J. Climatol.*, *28*, 667–678.

369 Meehl, G. A., J. M. Arblaster, D. M. Lawrence, A. Seth, E. K. Schneider, B. P. Kirtman,
370 and D. Min (2006), Monsoon regimes in the CCSM3, *J. Clim.*, *19*, 2482–2495.

371 Rayner, N. A., D. E. Parker, E. B. Horton, C. K. Folland, L. V. Alexander, D. P. Rowell, E.
372 C. Kent, and A. Kaplan (2003), Global analyses of sea surface temperature, sea
373 ice, and night marine air temperature since the late nineteenth century, *J. Geophys.*
374 *Res.*, *108*(D14), 4407, doi:10.1029/2002JD002670.

375 Shen, S., and K.-M. Lau (1995), Biennial oscillation associated with the East Asian
376 summer monsoon and tropical sea surface temperature, *J. Meteor. Soc. Japan*, *73*,
377 105–124.

378 Wang, B., R. Wu, and X. Fu (2000), Pacific-East Asian teleconnection: How does ENSO
379 affect East Asian climate?, *J. Clim.*, *13*, 1517–1536.

380 Wang, B., and T. Li (2004), East Asian monsoon-ENSO interactions. *East Asian*
381 *monsoon*, Chang C.-P., Eds., World Scientific Publishing: Singapore, 177–212.

382 Wang, B., I.-S. Kang, and J.-Y. Lee (2004), Ensemble simulations of Asian-Australian
383 monsoon variability by 11 AGCMs, *J. Clim.*, *17*, 803–818.

384 Wu, R., and B. Wang (2002), A contrast of the East Asian summer monsoon-ENSO
385 relationship between 1962-77 and 1978-93, *J. Clim.*, *15*, 3266–3279.

386 Wu, Z.-X., and R. E. Newell (1998), Influence of sea surface temperature on air

387 temperature in the tropics, *Clim. Dyn.*, 14, 275–290.

388 Xie, P., and P. A. Arkin (1997), Global precipitation: a 17-year monthly analysis based on
389 gauge observations, satellite estimates, and numerical model outputs, *Bull. Amer.*
390 *Meteor. Soc.*, 78, 2539–2558.

391 Yihui, D. (1994), *Mosoons over China*. Kluwer Academic Publishers: Dordrecht,
392 Netherlands.

393 Zhang, R., A. Sumi, and M. Kimoto (1996), Impact of El Niño on the East Asian
394 Monsoon: A diagnostic study of the '86/87 and '91/92 events, *J. Meteor. Soc.*
395 *Japan*, 74, 49–62.

396

396 **Figure captions**

397

398 **Fig. 1.** The monthly average El Niño SST anomalies from the Hadley Center monthly
399 SST data, which are used in the El Niño simulations.

400

401 **Fig. 2.** (a) Zonally averaged annual precipitation from CAM-CLM3 (dotted line) and
402 GPCP (solid line) and (b) their horizontal distributions and difference. Horizontal
403 distributions and differences of seasonal mean precipitation are shown in Figure S1 in the
404 auxiliary material.

405

406 **Fig. 3.** Comparisons of (a) precipitation (mm/day), (b) 150 hPa DIV (s^{-1}), (c) SLP (hPa),
407 (d) 500 hPa HGT (gpm), and (e) 850 hPa wind vectors (m/s) and vorticity (s^{-1} ; shaded)
408 for JJA between the control simulations (75-year average) and observations (25-year
409 average; 1979~2003). Precipitation is from GPCP and other variables are from NCEP-
410 DOE AMIP-II reanalysis. The boxes denote the NEASM region.

411

412 **Fig. 4.** Simulated differences of mean JJA (a) precipitation (mm/day), (b) 150 hPa DIV
413 (s^{-1}), (c) SLP (hPa), and (d) 500 hPa HGT (gpm) between the El Niño and control
414 simulations (left panels). Observed differences of those variables for the five years of
415 highest SST anomalies in the tropical eastern Pacific and normal year (right panels).
416 Significant regions at the 90 and 95% are contoured. The boxes denote the NEASM
417 region.

418

419 **Fig. 5.** Simulated differences of mean JJA 850 hPa wind vectors (m/s) and vorticity (s^{-1} ;

420 shaded) between the El Niño and control simulations (left panel). Composite
421 differences of those variables for the five years of both highest and lowest of SST
422 anomalies in the tropical eastern Pacific (right panel; same as in Figure 4(b) of *Lee et al.*,
423 2008). The boxes denote the NEASM region.

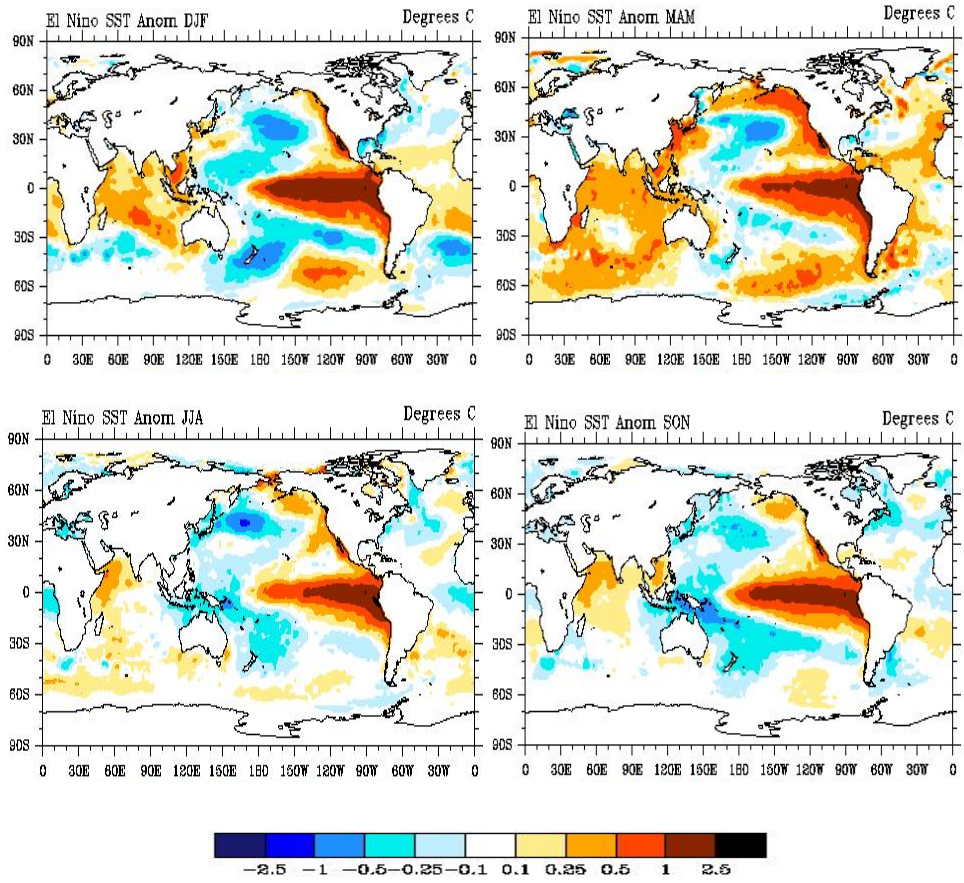
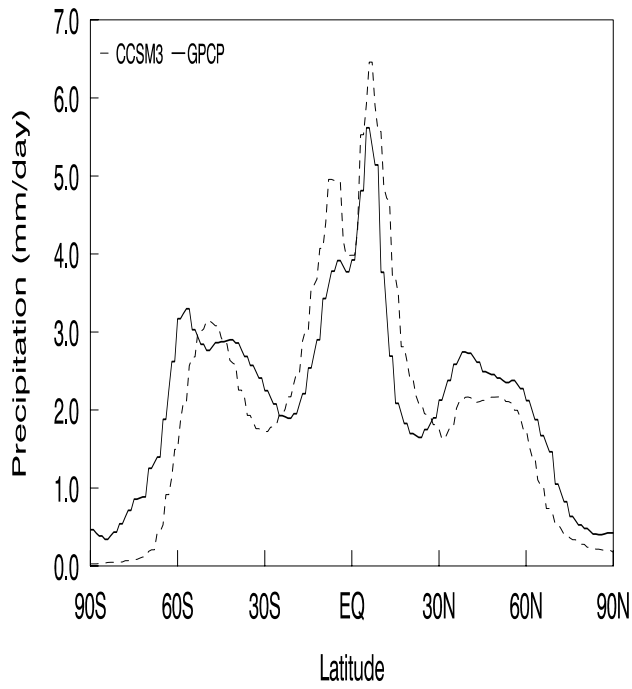


Fig. 1

(a) Zonal pattern



(b) Spatial patterns and their difference

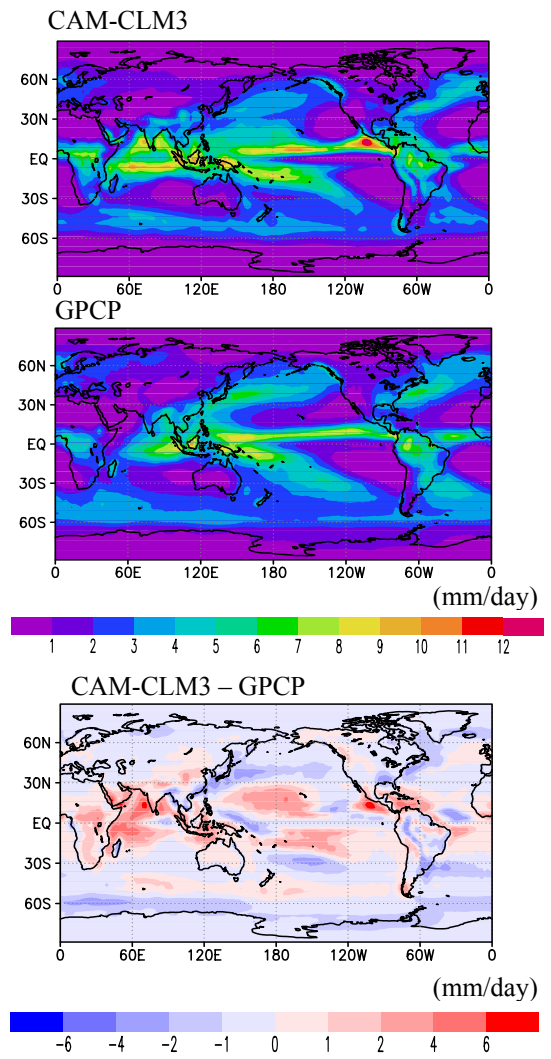
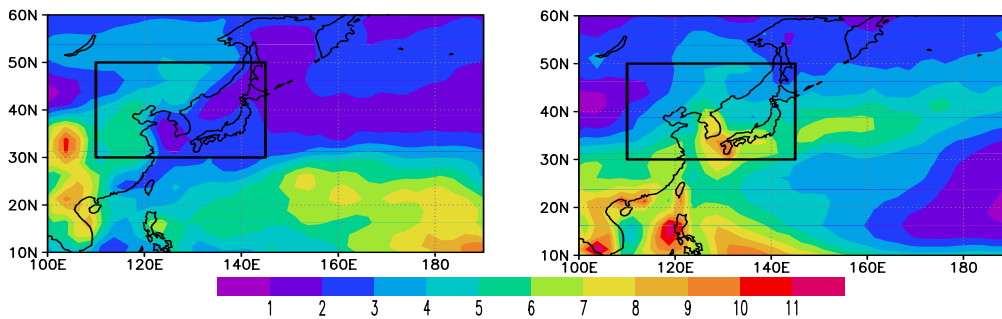


Fig. 2

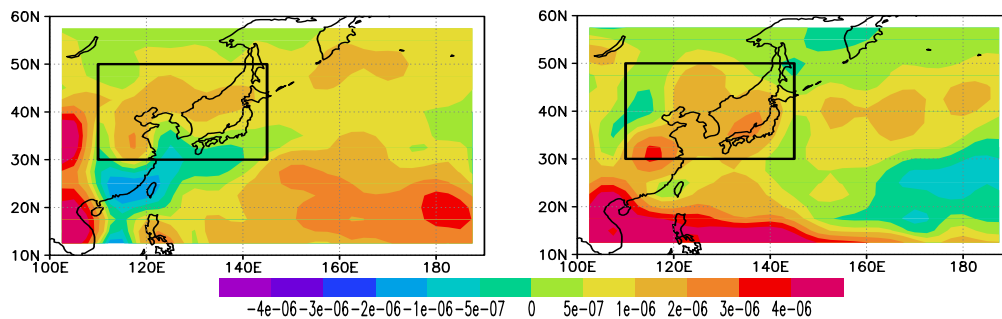
CAM-CLM3 controls

Observations

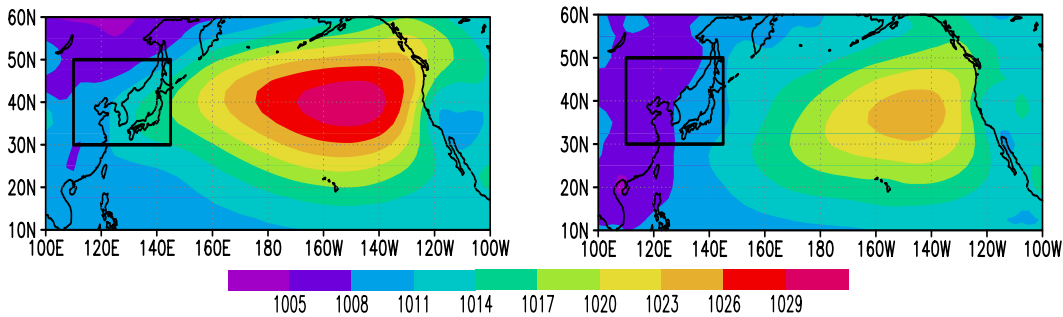
(a) Precipitation



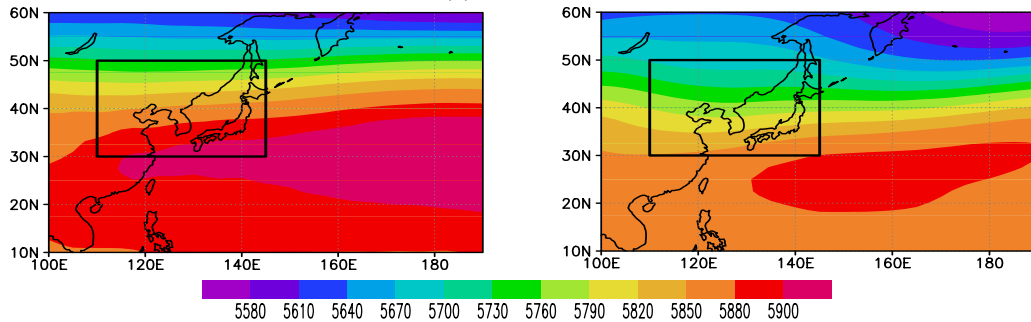
(b) 150 hPa DIV



(c) SLP



(d) 500 hPa HGT



(e) 850 hPa wind vectors and vorticity

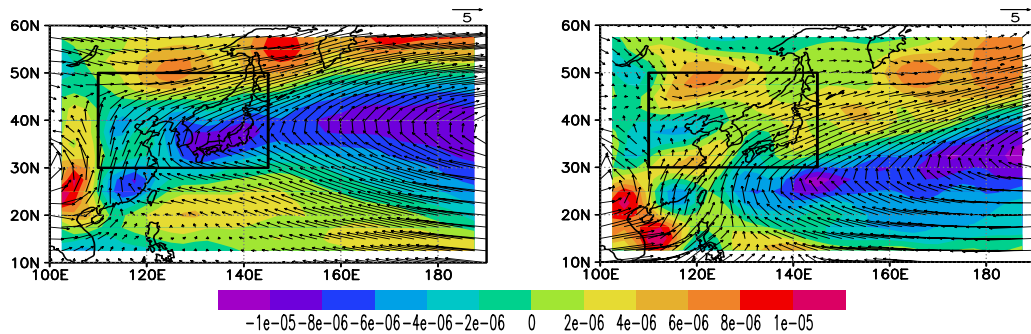
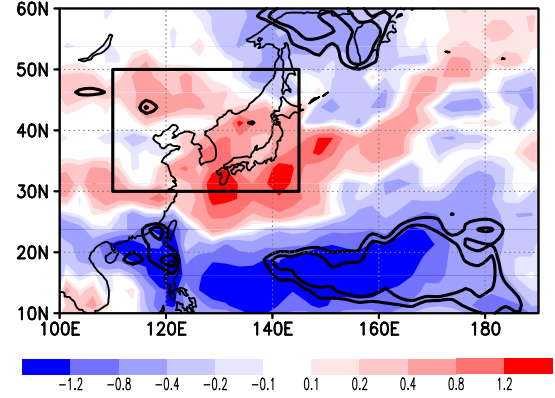
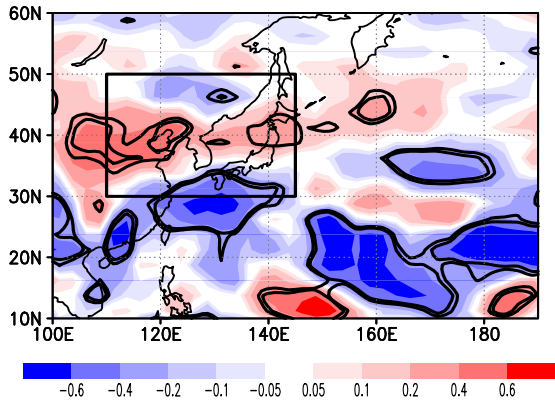


Fig. 3

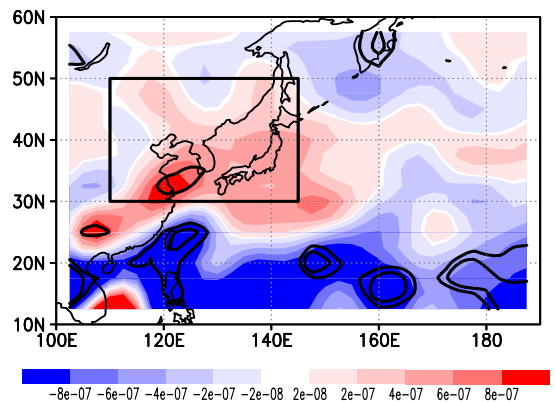
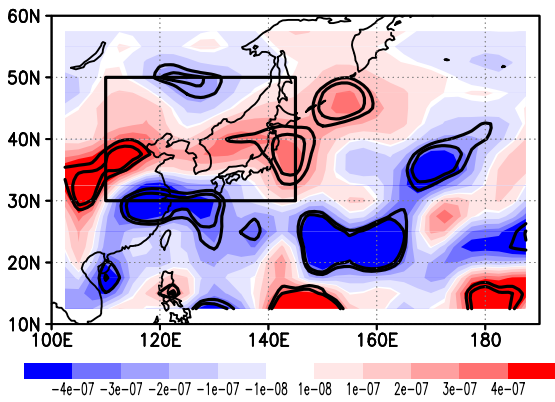
CAM-CLM3

Observations

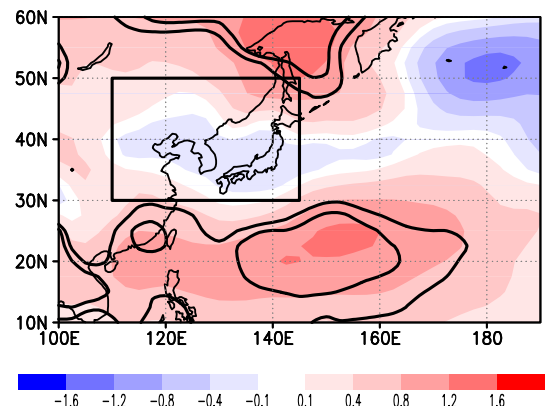
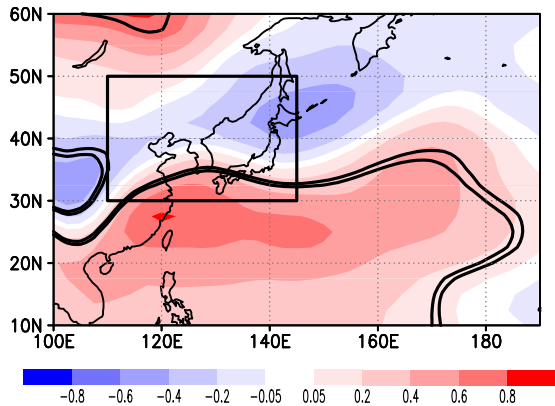
(a) Precipitation



(b) 150 hPa DIV



(c) SLP



(d) 500 hPa HGT

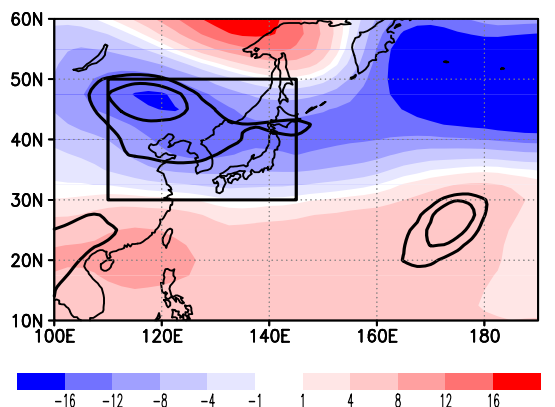
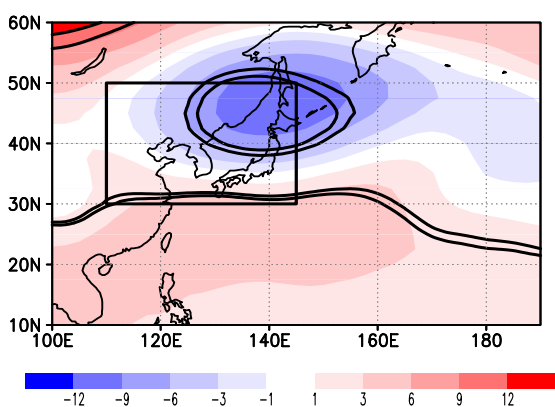


Fig. 4

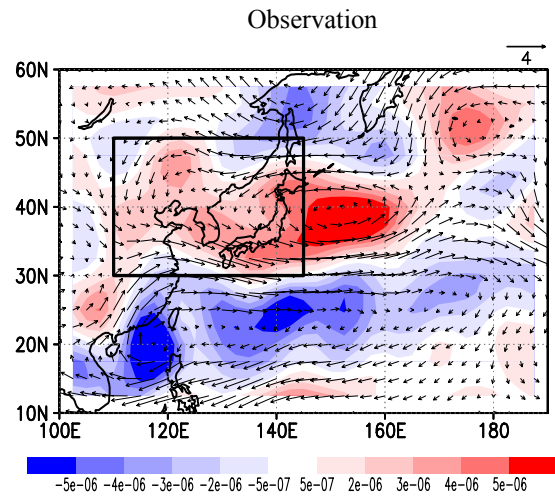
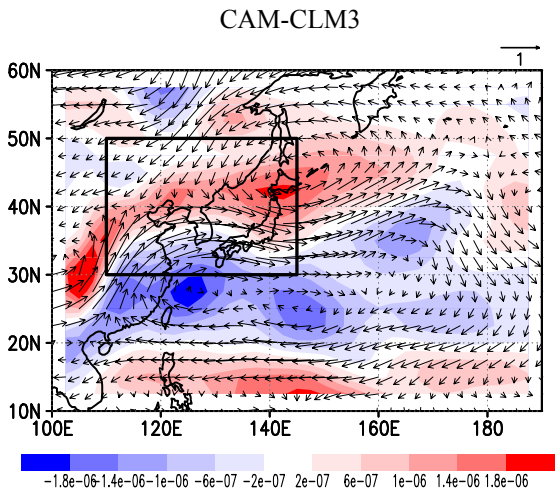


Fig. 5